

## Chapter 7

### Determination of potassium scattering lengths

The theory of photoassociation (PA) lineshapes developed in Chapter 6 is herein applied to analyze measured  $^{39}\text{K } 0_g^-$  rovibrational spectra. In particular, synthetic spectra are generated that reproduce most features of the experimental spectra. Requiring that the theoretical relative intensities and rotational linewidths agree with the experimentally measured counterparts, within experimental uncertainties, allowed us to place limits on the singlet and triplet  $s$ -wave scattering lengths. These results were first reported in Ref.[147]. Previous estimates of the K scattering lengths had in fact already appeared in the literature[148, 149]. However, the older works were based on conventional molecular spectroscopy. These data alone proved insufficient to reliably extrapolate the potentials to the dissociation threshold. The analysis presented here, which makes use of both the conventional spectroscopic data as well as the new photoassociation data, should therefore provide a more reliable prediction for the scattering lengths. In addition, an independent analysis[150] of the  $^{39}\text{K } 1_u$  spectra confirms many of the results presented here. This chapter is broken into two sections. First, an overview of the experiment is provided in Section 7.1. The analysis of the spectra and the resulting bounds on scattering lengths are presented in Section 7.2.

#### 7.1 Photoassociation experiment

The experiment discussed here was conducted by H. Wang, P. L. Gould, and W. C. Stwalley at the University of Connecticut. They have published complete details of the experimental setup in Ref.[144, 146]. This section provides a brief description of those experimental details that are necessary to understand the analysis presented in Section 7.2. In particular, the experimental checks taken to ensure the quality of the data are emphasized.

A sample of  $10^7$   $^{39}\text{K}$  atoms, at a density greater than  $10^{11} \text{ cm}^{-3}$  and a temperature of  $\sim 400\mu\text{K}$ , are prepared in a “dark spot” vapor cell magneto-optical trap (MOT). The atoms are trapped predominately in their  $f_a = 1$  hyperfine state (for  $^{39}\text{K}$ ,  $i_a = 3/2$ ). Separate single-mode tunable ring Ti:sapphire lasers provide the trapping beams and induce the PA transitions. The total output power of the

trapping laser is  $\sim 300$  mW at 766.5 nm while the PA laser intensity is typically  $50$  mW/cm<sup>2</sup>. The analysis presented in Section 7.2 concentrates on the  $v' = 0-6$  vibrational levels of the  $0_g^-$  state. For these low lying states, trap loss spectra are not easily observed because the local kinetic energy is not large enough to allow atoms to escape from the trap when the excited vibrational state decays through bound-free spontaneous emission of a photon. The PA resonances can then be detected by recording ion production following a double-resonance transition from the  $0_g^-$  rovibrational state to an autoionizing  $1_u$  state at an energy below the highly excited  $4S + nD$  ( $n = 5$  or  $6$ ) asymptote[151]. In particular, a tunable ring dye laser provides the second photon, at frequency  $\nu_2$  and typical intensity  $12$  W/cm<sup>2</sup>, for the double-resonance process and a channeltron multiplier records the subsequent production of ions. A schematic of the transition steps is provided in Fig. 7.1.

Unfortunately, there is essentially no information on the excited state potentials  $4S + nD$ , which prevents us from applying the two-color theory presented in Ref.[134, 135]. It was therefore necessary to ascertain the influence of the second laser on the PA spectrum of the  $0_g^-$  state experimentally. These tests included recording spectra using final autoionizing states below both the  $4S+5D$  and  $4S+6D$  asymptotes. Representative examples of these spectra are shown in Fig. 7.2. The autoionizing final states are structureless and broad[151] with widths ranging from  $\sim 1$  GHz for levels near the  $4S+5D$  threshold to  $\sim 2$  GHz for levels near the  $4S+6D$  asymptote. General trends in the PA spectra of the  $0_g^-$  state, such as weak or missing odd  $J'$  rotational levels, anomalous  $J' = 2$  linewidths, and large  $J' = 4$  relative intensities were consistent in both cases. The only noticeable differences occur in the  $J' = 4$  relative intensity which was typically a factor of 1.5-2 bigger in the spectra observed using final states below the  $4S + 6D$  threshold. This difference can apparently be attributed to slightly hotter atoms in the MOT for the  $4S + 6D$  experiment (based on linewidths), and to the broader final state that experiment.

PA spectra of the  $0_g^-$  state were measured by fixing the second laser frequency  $\nu_2$  to a  $0_g^-(v'J' = 2) \rightarrow 1_u(v)$  transition near the  $4S+nD$  asymptote, then scanning the PA laser frequency ( $\nu_1$ ). Altering this setup so that  $\nu_2$  was tuned from  $J' = 0$  or  $J' = 4$  to the final autoionizing state again produced no qualitative changes in the measured  $0_g^-$  spectra. The only quantitative difference again appeared in the  $J' = 4$  relative intensities. These were roughly a factor of 1.5 larger when the second laser was tuned from  $J' = 4$  instead of  $J' = 0$  or  $2$  (see Fig. 7.3). Changing the power of laser  $\nu_2$  only affected the total ion production rate. In addition, the experimentalists varied the PA laser intensity by a factor of two and observed no noticeable power broadening. Based on this near independence of the spectra on the second laser, we attribute the bulk of the relative peak intensities to the first transition. The single color theory presented in Chapter 6 should therefore provide a good approximation to the measured lineshapes.

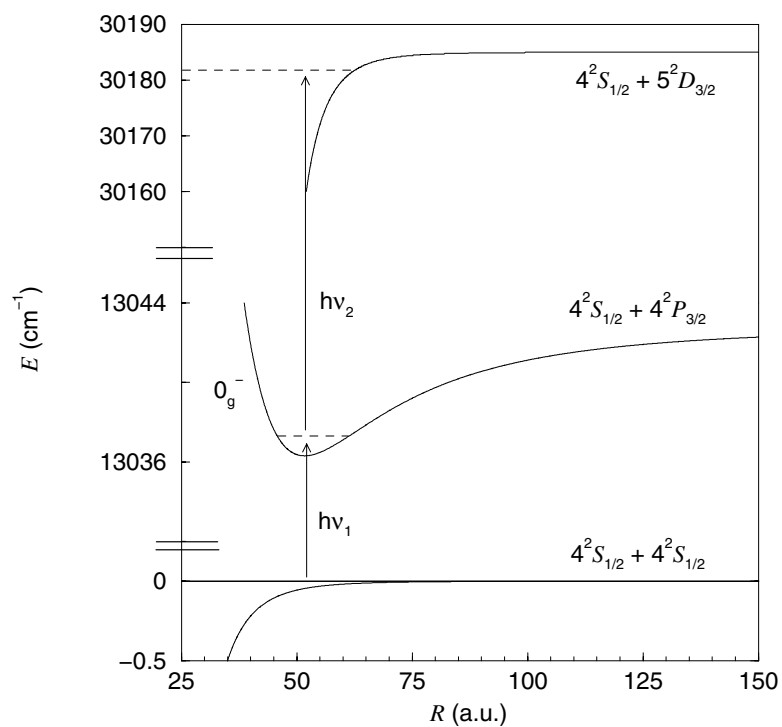


Figure 7.1: Schematic of the  $^{39}\text{K}$  photoassociation transition sequence. Ground state atoms are first excited ( $h\nu_1$ ) to a rovibrational level of the  $0_g^-$  electronic state. The free-bound transition is detected by exciting the molecule at frequency  $\nu_2$  to an autoionizing state below either the  $4S + 5D$  or  $4S + 6D$  threshold and then measuring the resulting production of ions.

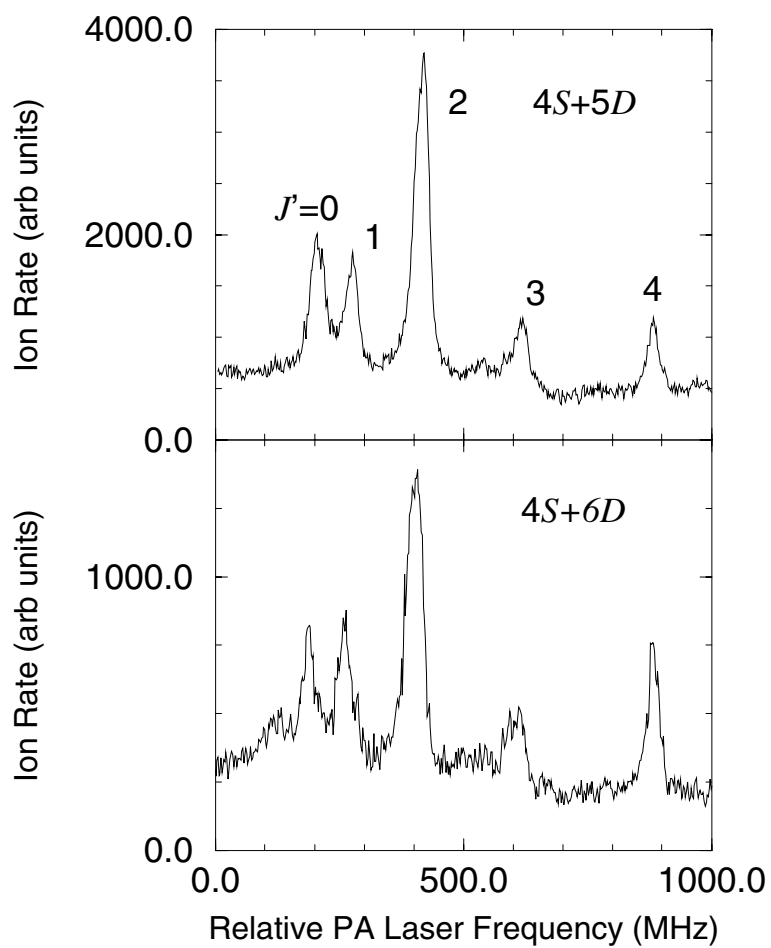


Figure 7.2: Representative examples of the  $0_g^- v'=0$  spectra obtained using autoionizing final states below the  $4S + 5D$  and the  $4S + 6D$  thresholds. The rotational assignment  $J'$  for each peak is indicated in the top graph.

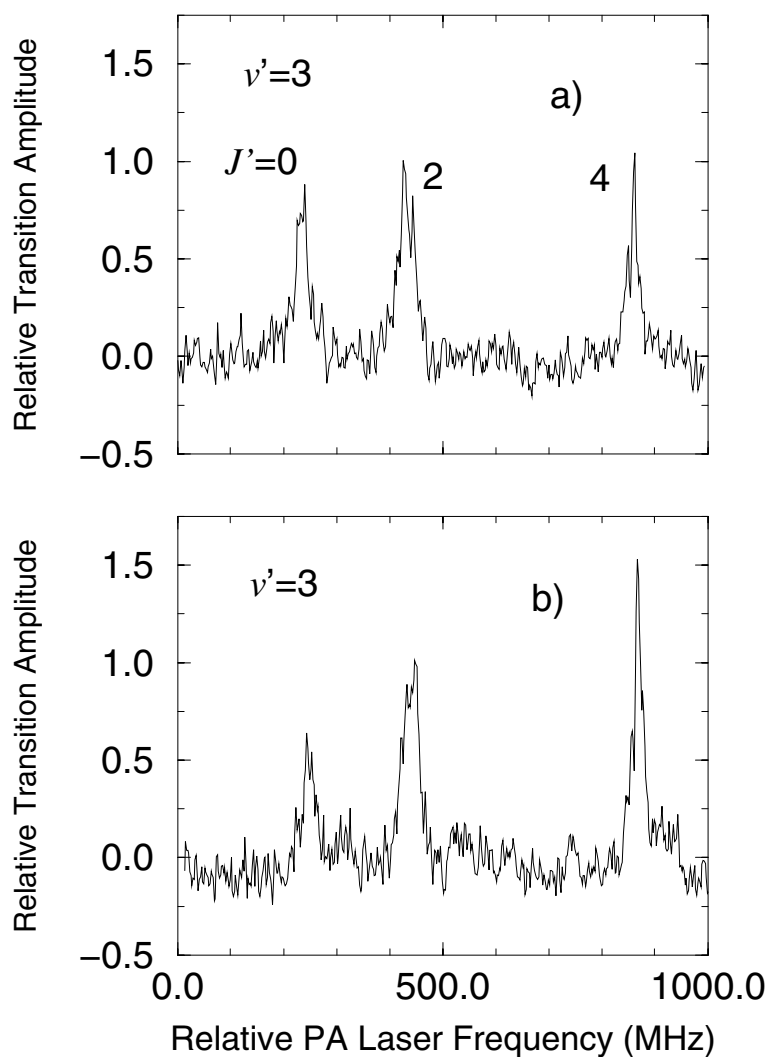


Figure 7.3: Representative examples of the  $0_g^- \nu'=3$  spectra obtained for different values of  $\nu_2$ . The peaks correspond to the  $J' = 0, 2, 4$  rotational levels, respectively.  
 a)  $\nu_2$  fixed to a  $0_g^-(J'=2) \rightarrow 1u(\nu)$  transition near the  $4S + 6D$  asymptote.  
 b)  $\nu_2$  fixed to a  $0_g^-(J'=4) \rightarrow 1u(\nu)$  transition near the  $4S + 6D$  asymptote.

## 7.2 Analysis

The analysis of the  $0_g^-$  spectra is simplified somewhat by its symmetry rules. These were discussed briefly in Section 6.2 and are elaborated on here. The parity of a  $0_g^-$  rotational wave function is  $(-1)^{J'+1}$ , while the ground state wave function parity is simply  $(-1)^l$ . Therefore, dipole selection rules restrict transitions from ground state collisions in even partial waves  $l$  to even rotational levels  $J'$  and likewise odd partial waves to odd  $J'$ 's. More specifically,  $s$ -wave collisions contribute to  $J' = 0, 2$ ;  $d$ -wave collisions contribute to  $J' = 0, 2, 4$ ; and  $p$ -wave collisions contribute only to  $J' = 1, 3$ . In addition the  $0_g^-$  electronic state for like atoms has a nuclear permutation symmetry which requires  $(-1)^{J'+I'}$  to be odd.

The measured spectra show several distinct trends. First, the  $p$ -wave features are extremely weak or missing from all vibrational scans except  $v' = 0$  and 2. Second, the relative intensity of the  $J' = 4$  (pure  $d$ -wave) peak is found to be quite large in all the scans. This is surprising since the height of the  $^{39}\text{K}$   $d$ -wave centrifugal barrier is roughly 1.5 mK and at cloud temperatures around 400  $\mu\text{K}$  one would expect, in the absence of resonances, the  $d$ -wave features to be suppressed by the Wigner threshold law. Finally, the  $J' = 2$  linewidths are quite large  $\sim 35$  MHz compared to the other rotational lines  $\sim 25$  MHz. The analysis of the measured data will focus on these particular features.

Suppressed  $p$ -wave features were also observed[136] in the Na  $0_g^-$  spectra. However, in sodium the Franck-Condon overlap was controlled essentially by a node in the open channel wave function. In potassium, the closed channel wave functions can contribute substantially to the transition, as can be seen from Fig. 7.4. The Franck-Condon contribution from each channel must be added coherently (Eq. 6.37), which can contribute to the suppressed  $p$ -wave features. The outer turning points of the closed channel potentials occur at roughly the same internuclear separation as the inner turning point of the excited state potential. This means that the closed channels, which are on their last half cycle at the Condon point, can have a large effect on the radial overlap integral. Moreover, the shapes of the closed channel wave functions near the Condon point are essentially “fixed” in  $R$ , as they must begin their exponential decay. Varying the singlet and triplet scattering lengths thus only affects the relative amplitudes in the channels. For example, the amplitudes will be quite small when  $a_s \sim a_t$  just as  $^{87}\text{Rb}$  spin exchange inelastic rates[100] are suppressed by this criterion. It is therefore not obvious (or unique) where the open channel node needs to be placed in order to reproduce the observed suppression of the  $p$ -wave features.

This complication prompted us to perform a complete search of singlet-triplet scattering length space to ensure that our final fits to the spectra provided a unique set of parameters. The ground state potentials were systematically varied (Eq. 2.45) such that the singlet  $a_s$  and triplet  $a_t$  scattering lengths ranged between  $\pm\infty$ . This search was also conducted for a number of different  $C_6$  coefficients rang-

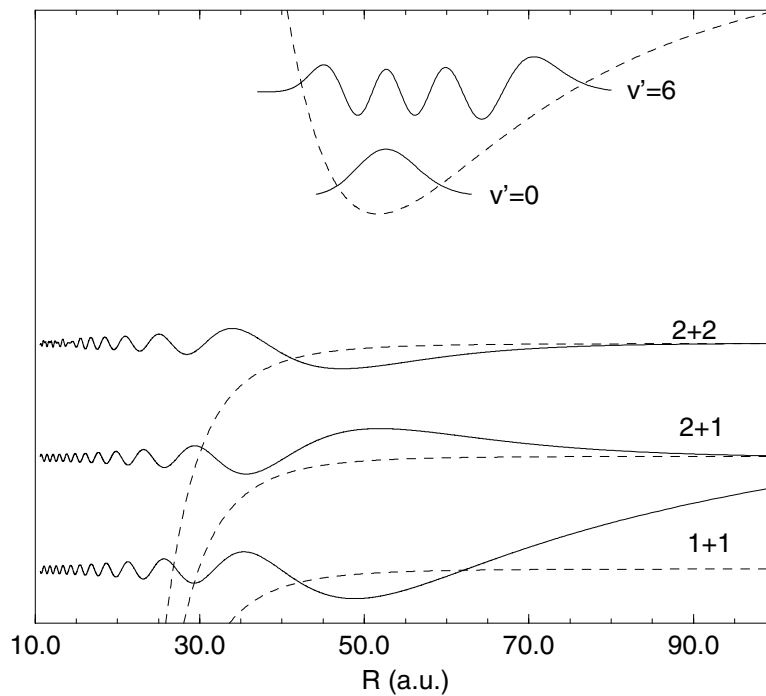


Figure 7.4: Schematic of the ground and excited state potentials (dashed lines) and wave functions (solid lines). The ground state thresholds are labeled by their  $f_a + f_b$  quantum numbers. The ground state wave functions are computed at zero energy. The excited state wave functions correspond to the lowest and highest vibrational levels ( $v' = 0$  and  $6$ , respectively) used in the analysis. Notice that the closed channel components of the ground state wave function can contribute significantly to the Franck-Condon overlap with the excited state wave function. The potentials are not shown to scale.

ing from 3600-4000 a.u., to allow for the stated  $\pm 5\%$  uncertainty given in Ref.[38]. Ground state wave functions for each set  $(a_s, a_t, C_6)$  of potentials were generated using the MQDT method outlined in Section 4.2 (see also Section 6.3.2 for a discussion of the ground state wave functions needed for this analysis). For each set of potentials, a thermally averaged synthetic rotational  $J'=0-4$  series was generated for vibrational levels  $v'=0-6$  (equations 6.5 and 6.37). A “match” to the measured data required that the theoretical relative intensities and linewidths of a rotational progression within a given  $v'$  agree within experimental bounds simultaneously for each vibrational level  $v'=0-6$ . A constant cloud temperature, estimated to be  $400 \pm 100 \mu\text{K}$  from fits to the measured spectra, was assumed for each vibrational level. Absolute intensities are quite uncertain, therefore each vibrational spectrum was normalized to  $K_p^{\text{max}}(J'=2) = 1$ . In addition, the absolute PA laser frequency  $\nu_1$  was adjusted such that the blue edge of the synthetic and measured  $J'=2$  lines are aligned for each vibrational spectrum. The absolute intensity and absolute frequency are the only two adjustable fit parameters incorporated into the theory.

The data obtained from the  $4S + 6D$  autoionizing final state was used exclusively in this analysis. The uncertainties associated with the second laser were better characterized for this data and therefore more precise bounds could be placed on the scattering lengths. A comparison of spectra calculated with our “nominal” set of potentials is shown in Fig. 7.5. The  $J'=4$  relative intensity is the main discrepancy between experiment and theory. This can be attributed to optimizing the double resonance experiment using the  $J'=2$  intermediate level which then under represents the  $J'=4$  intensities (see Fig. 7.3). The final values for the singlet and triplet scattering lengths, as well as quantum defects, are given in Table 7.1. The table also translates these results into scattering lengths for other K isotopes. In addition, a table of K atomic parameters is provided (Table 7.2).

In the following discussion, the contribution of each spectral feature to the final limits placed on either the singlet or triplet scattering length is slightly artificial. Bear in mind that it is only through the combination of these features that unique limits on  $a_s$  and  $a_t$  are obtained. The large  $J' = 2$  linewidths are a particularly interesting feature. We find that these linewidths are a result of a broad  $f=0$   $d$ -wave shape resonance, at an energy  $E_R = 1.15 \pm 0.35$  mK with a width  $\Delta = 0.5 \pm 0.2$  mK (the time-delay definition of position and width has been used here, see Eq. 5.5). The  $J' = 2$  spectral width provides a fairly sensitive probe of the position of the shape resonance. Figure 7.6 shows the effect on the  $J' = 2$  linewidth as the position of the shape resonance is varied. Recall that atoms scattering in both  $s$  and  $d$  partial waves contribute to the intensity of the  $J' = 2$  rotational level. Moving  $E_R$  to larger energies shifts the  $d$ -wave contribution to the red of the  $s$ -wave contribution, thereby increasing the overall width. However, if  $E_R$  becomes too large relative to the cloud temperature, the thermal averaging suppresses the  $d$ -wave intensity contribution effectively reducing the linewidth. Similarly, if  $E_R$  is moved to smaller energies not only is the red shift reduced but the  $d$ -wave contribution

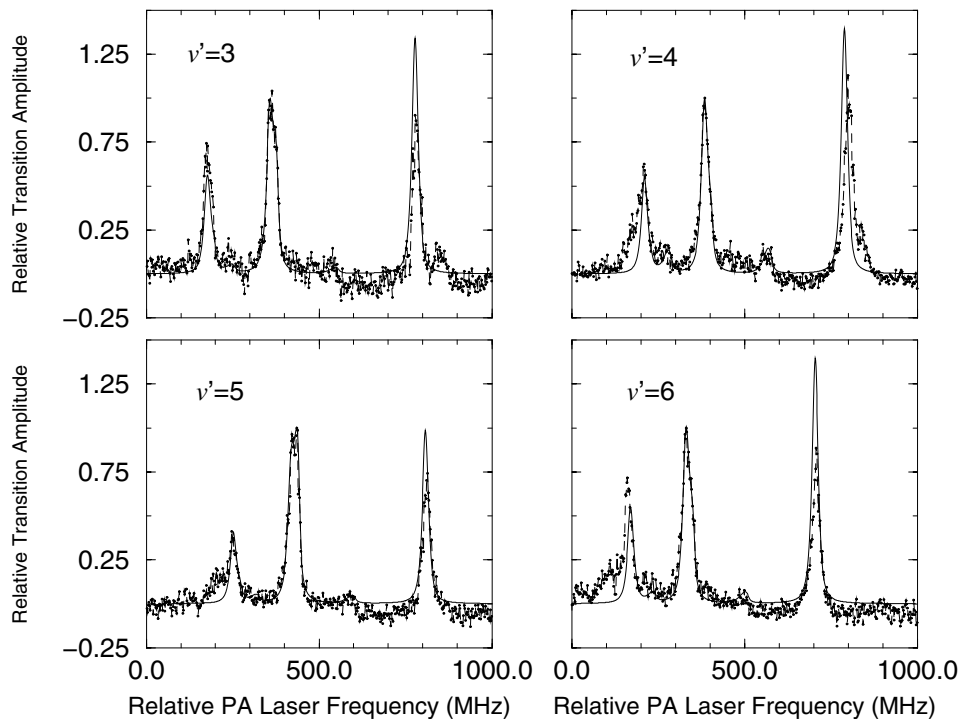


Figure 7.5: Comparison of experimental (dashed line) and theoretical (solid line) spectra. The synthetic spectra were calculated using our nominal set of potentials,  $a_s = 140$  a.u.,  $a_t = -17$  a.u. and  $C_6=3800$  a.u., assuming a cloud temperature of  $400 \mu\text{K}$ . The prominent peaks in each vibrational spectra are the rotational levels  $J' = 0, 2, 4$ , reading from left to right. It is believed that the red wing of the  $J' = 0$  experimental peaks correspond to additional flux obtained from  $f_a=1 + f_b=2$  collisions. These collisions were not theoretically modeled since they contribute little to the spectrum.

Table 7.1: Singlet and triplet scattering lengths  $a$  (in a.u.) and quantum defects  $\mu$  (dimensionless) for collisions among different pairs of potassium isotopes assuming a constant  $\bar{C}_6=3800$  a.u. The scattering length is related to the quantum defect by:  $a = -C^2 \tan(\pi\mu)/(1 + \mathcal{G}(0) \tan(\pi\mu))$  where  $C^2 = 0.95775(2mC_6)^{1/4}$ ,  $m$  is the reduced mass of the atom-pair and  $\mathcal{G}(0) = -1.0037$ . The singlet quantum defect uncertainties are  ${}^{+0.019}_{-0.011}$  for each collision pair, independent of the  $C_6$  value. Finally, the uncertainties associated with each triplet quantum defect and its variation with  $C_6$  is given by:  $\mu_t = \bar{\mu}_t + 8.0(10^{-5})(C_6 - \bar{C}_6) {}^{+0.04}_{-0.06}$ .

Isotopes	$a_s$	$\bar{\mu}_s$	$a_t$	$\bar{\mu}_t$
39 + 39	$140^{+6}_{-9}$	0.460	$-17 \pm 25$	0.039
40 + 40	$105^{+3}_{-5}$	-0.445	$194^{+114}_{-35}$	0.388
41 + 41	$85 \pm 3$	-0.366	$65^{+13}_{-8}$	-0.268
39 + 40	$-1^{+4}_{-8}$	0.002	$-460^{+330}_{-\infty}$	0.212
39 + 41	$113 \pm 5$	-0.474	$205^{+140}_{-40}$	0.379
40 + 41	$-50^{+9}_{-18}$	0.089	$104^{+20}_{-11}$	-0.441

Table 7.2: Mass in  ${}^{12}\text{C}$  amu, nuclear spin  $i$ , nuclear g-factor  $g_n$ , and ground-state atomic hyperfine splittings of the K isotopes. A negative value of  $\Delta$  indicates an “inverted” hyperfine structure.

Isotope	Mass	$i$	$g_n$	$\Delta$ (MHz)
39	38.963707	3/2	0.39146	461.72
40	39.963999	4	-1.298	-1285.79
41	40.961825	3/2	0.21487	254.01

with its extra  $(2l+1)$  phase space factor overwhelms the  $s$ -wave contribution, again resulting in a smaller linewidth. The large  $J' = 4$  peaks are also a by-product of this shape resonance and their relative intensities are quite sensitive to the position of the resonance.

These constraints force  $E_R$  to lie in the range  $1.15 \pm 0.35$  mK, which creates an “allowed” strip in Fig. 7.7. In particular, the position of the resonance depends sensitively on the singlet scattering length and thus imposes tight bounds on this quantity. However, because the resonance is near the top of the centrifugal barrier and therefore quite broad, the spectral linewidths are relatively insensitive to the  $C_6$  value. In fact, we find the bounds on the singlet scattering length are unchanged when  $C_6$  is allowed to vary between 3600-4000 a.u. Allowing a quarter linewidth uncertainty on each  $J' = 2$  peak, places the following bounds on  $a_s = 140_{-9}^{+6}$  a.u., which is in good agreement with Ref.[149]. Comparison of the  $J' = 2$  measured linewidths with our “best” fit potentials are shown in Fig. 7.8. Finally, it should be noted that this  $f = 0$   $d$ -wave shape resonance manifests itself in other features seen in the  $1_u$  spectra[150]. However, we do not agree on the exact position of the resonance and therefore have different constraints on the singlet scattering length. We believe this discrepancy indicates a limitation of the “naive” PA theory (which was also applied to the  $1_u$  spectra) that disregards the effect of the ionizing laser. This point is discussed in more detail in Ref.[150].

There is, in fact, another bound on  $E_R$ . Raising  $E_R$  above  $\sim 1.3$  mK introduces an additional  $f = 2$   $g$ -wave shape resonance[150]. The existence of a  $g$ -wave resonance should manifest itself in the  $0_g^-$  spectrum as an additional  $J' = 6$  peak (as well as contributing to  $J' = 2$  and 4). However, there is no experimental evidence for an additional rotational peak. Also, the presence of a  $g$ -wave resonance would be inconsistent with the  $1_u$  spectra[150]. The exclusion of the  $g$ -wave resonance thus reduces slightly our allowed parameter space (see Fig. 7.7).

Placing bounds on  $a_t$  is more complex. The suppression of the  $p$ -wave features ultimately controls the allowed  $a_t$  range, but it is only after limiting the available parameter space by considering the  $d$ -wave shape resonance that we find an unambiguous result. However, these combination of features require that the wave function nodes are bounded as follows:  $f=1$ ,  $p$ -wave node  $68_{-6}^{+9}$  a.u. and the  $f=2$ ,  $s$ -wave node is  $62_{-3}^{+4}$  a.u. The positions of these nodes in our allowed  $a_s$ - $a_t$  parameter space are controlled almost exclusively by the triplet scattering length. Unfortunately the suppression of the  $p$ -wave features is fairly robust in this region which is largely responsible for the bigger uncertainty in the triplet scattering length. Variations in  $C_6$  require a corresponding change in the triplet scattering length to preserve the nodal positions. We found changing the value of the  $C_6$  coefficient simply shifted our allowed parameter region along the triplet axis of the  $a_s$ - $a_t$  plane while preserving the area. The triplet scattering length is therefore parameterized in the following manner  $a_t = -17 - 0.045(C_6 - \bar{C}_6) \pm 25$  a.u.,  $\bar{C}_6 = 3800$ . The two most important scattering lengths for BEC are the triplet scattering length  $a_t$  and the

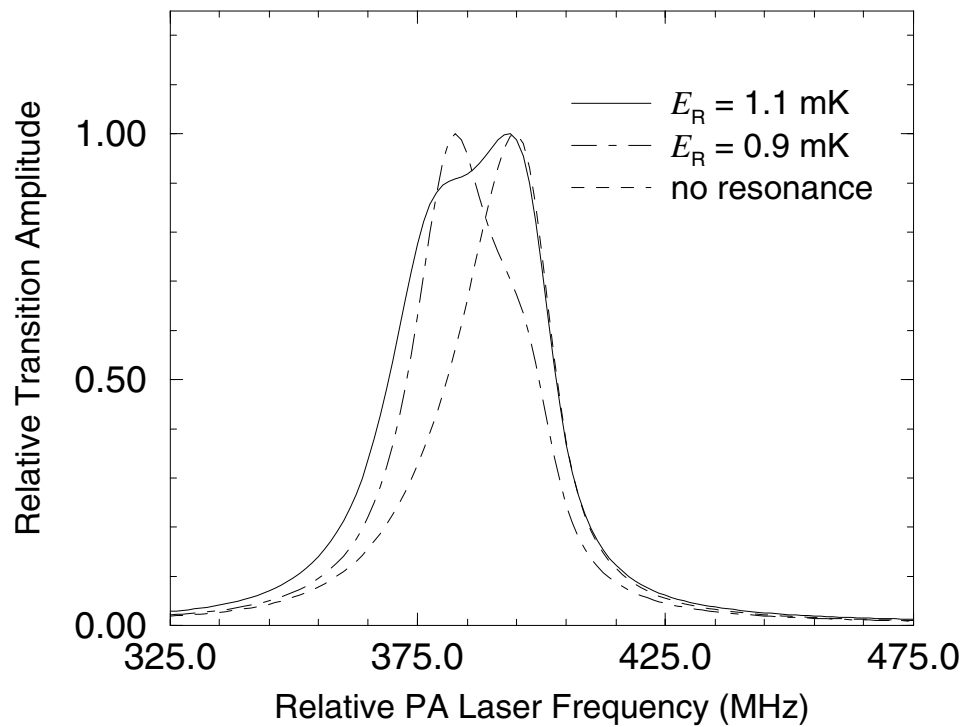


Figure 7.6: Comparison of the  $J' = 2$  linewidths versus the position  $E_R$  of the  $f=0$   $d$ -wave shape resonance. The no resonance case indicates the  $s$ -wave contribution to the linewidth. The position of the resonance controls the relative  $d$ -wave contribution to the peak and the amount it is red-shifted relative to the  $s$ -wave contribution.

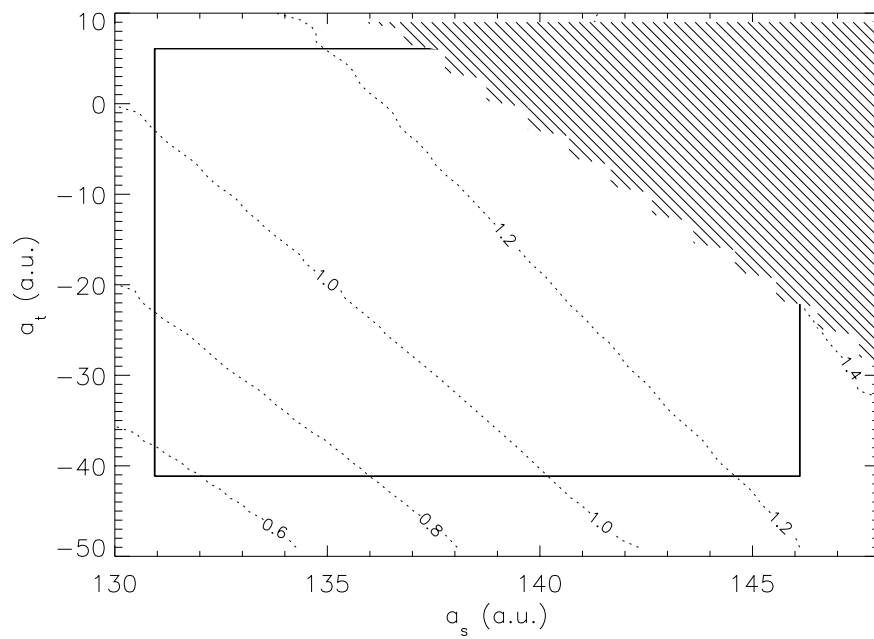


Figure 7.7: The dashed lines indicate the energy position  $E_R$  (in mK) of the  $d$ -wave shape resonance in the  $a_s$ - $a_t$  plane. The solid rectangle represents our allowed individual singlet and triplet parameter ranges ( $C_6 = 3800$  a.u.) including the  $\pm 100$   $\mu\text{K}$  uncertainty in cloud temperature. The hatched region indicates the parameter space excluded by the absence of the  $f = 2$   $g$ -wave shape resonance.

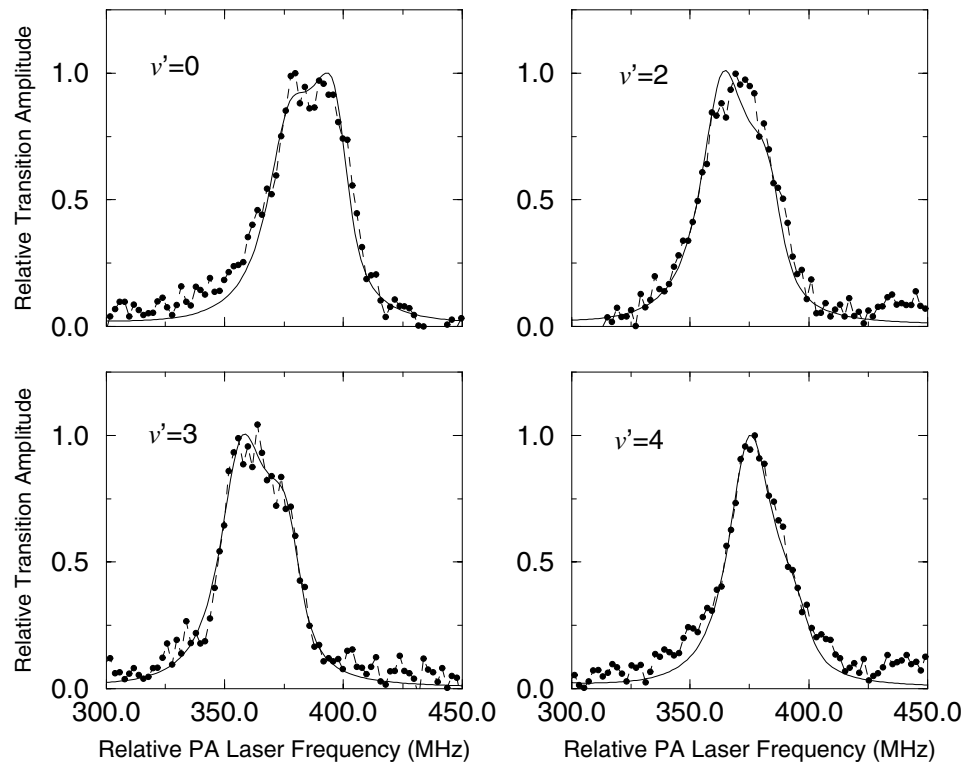


Figure 7.8: Comparison of experimental (closed circles) and theoretical (solid line)  $J' = 2$  linewidths. The synthetic spectra was calculated using our nominal set of potentials,  $a_s = 140$  a.u.,  $a_t = -17$  a.u. and  $C_6 = 3800$  a.u., assuming a cloud temperature of  $400 \mu\text{K}$ .

$f = 2$   $s$ -wave scattering length  $a_{2s}$ . From our final potentials, we find  $a_{2s} = -20 - 0.055(C_6 - \bar{C}_6) \frac{+35}{-45}$  a.u. Both  $a_t$  and  $a_{2s}$  are in agreement with the results from the  $1_u$  analysis[150]. In addition, our  $^{40}\text{K}$  triplet scattering length is consistent with the value extracted from a recent elastic scattering measurement[119]. Finally, we have used these refined Born-Oppenheimer potentials to survey the threshold scattering properties of a number of K hyperfine-selected states. These considerations were reported in Ref.[152].